Mapping of two-polarization-mode dynamics in vertical-cavity surface-emitting lasers with optical injection

I. Gatare,[1] M. Sciamanna,[2] M. Nizette,[3] H. Thienpont,[1] and K. Panajotov[1]
[1]*Department of Applied Physics and Photonics, Vrije Universiteit Brussel, 2 Pleinlaan, B-1050 Brussels, Belgium*
[2]*Supélec, LMOPS, CNRS UMR-7132, 2 Rue Edouard Belin, F-57070 Metz, France*
[3]*Optique Non Linéaire Théorique, Université Libre de Bruxelles (U.L.B.), CP 231 Boulevard du Triomphe, 1050 Bruxelles, Belgium*
(Received 6 November 2008; revised manuscript received 16 February 2009; published 28 August 2009)

We report theoretically on the interplay between polarization switching and bifurcations to nonlinear dynamics in a vertical-cavity surface-emitting laser (VCSEL) subject to orthogonal optical injection. Qualitatively different bifurcation scenarios leading to polarization switching are found and mapped out in the plane of the injection parameters, i.e., the frequency detuning vs injection strength plane. A Hopf bifurcation mechanism on the two-polarization-mode solution determines the injection-locking boundaries and influences polarization switching induced by optical injection. We furthermore report on a torus bifurcation emerging from a two-linearly polarized (LP) mode time-periodic dynamics before polarization switching and injection locking appear. It corresponds to an interesting combination of relaxation oscillation dynamics in the *x*-LP mode together with wave mixing dynamics in the injected *y*-LP mode. In agreement with recent experiments, we unveil a period-doubling route to chaos that involves both VCSEL orthogonal LP modes. The corresponding region of chaotic dynamics coincides with abrupt changes in the polarization switching boundaries in the plane of the injection parameters.

DOI: 10.1103/PhysRevE.80.026218 PACS number(s): 05.45.−a, 42.65.Sf

I. INTRODUCTION

Semiconductor lasers subject to external optical injection can exhibit nonlinear dynamics which are attractive in a range of applications dealing with optical communications. Under injection-locking conditions, improvement of lasing operation properties has been demonstrated in edge-emitting lasers (EEL): reduction in frequency chirp under modulation [1], laser spectral narrowing [2], suppression of mode partition noise [3], and modulation bandwidth enhancement [4]. Optical injection in semiconductor lasers can also be used to address a number of applications including all-optical signal processing [5], microwave generation [6], and wavelength add-drop functionalities for optical communication systems [7]. From the fundamental viewpoint, rich and complex nonlinear dynamics such as period-one oscillations [8], period-three limit cycles [9], subharmonic resonance [10], wave mixing, and deterministic chaos [11,12] have been extensively investigated in optically injected EEL. Detailed bifurcation studies have yielded a unified view which reveals how qualitatively different dynamical regimes may interconnect in a very intricate way when changing the injection parameters [13–15], i.e, the injection power and the frequency detuning between the master and the slave laser.

The study of optical injection in semiconductor lasers has recently been extended to vertical-cavity surface-emitting lasers (VCSELs). The growing interest in VCSELs is due to their competitive performances in the following areas: circular output beam with narrow divergence, low threshold current, and the possibility to fabricate dense two-dimensional VCSEL arrays for optical network interconnects [16]. Single-mode VCSELs typically emit a linearly polarized (LP) light aligned along one of two preferential orthogonal crystallographic axes (*x* and *y*). However, a change in their operating conditions, such as bias current or temperature, may induce polarization switching (PS) between the orthogonal LP states [17]. PS may also be induced by external perturbations such as current modulation, delayed optical feedback [18], or optical injection [19]. In spite of the fact that VCSEL polarization instabilities are major drawbacks for polarization-sensitive applications, they can also turn out to be useful in areas such as all-optical switching [20] or optical signal processing [21].

In their pioneering experimental work, Pan *et al.* have investigated in particular the polarization switching properties of a VCSEL subject to orthogonal optical injection [19]. In this configuration, the external light has polarization which is linear and orthogonal to that of the free-running VCSEL. They have demonstrated that PS induced by optical injection is achieved with bistability. In agreement with the experiments carried out by Pan. *et al.*, theoretical studies [22,23], based on the so-called spin-flip model (SFM) [24,25], have successfully reproduced the bistable PS behavior and its dependence on the injection parameters. Furthermore, the same studies [22,23] reported on the existence of two qualitatively different injection-locked solutions and also predicted complex nonlinear polarization dynamics induced by orthogonal optical injection. Recent experiments have confirmed the existence of nonlinear dynamics accompanying polarization switching in a VCSEL subject to orthogonal optical injection [26,27]. In particular, they showed that PS may be accompanied by a period-doubling (PD) route to chaos and that the onset of these nonlinear dynamics appears in the detuning conditions for which PS is achieved with minimum injected power. Recently, a two-polarization-mode time-periodic dynamics accompanying PS with injection locking has been found in [28].

In this paper we extend the theoretical results reported in Ref. [28] and provide comprehensive investigations of the interplay between polarization switching and nonlinear dy-

namics induced by optical injection in VCSELs. By mapping qualitatively different bifurcation curves on the injection parameter plane (the detuning versus optical injection strength plane), we can follow how the system dynamics and the switching mechanisms are organized and interconnected on a more global scale. We report on a Hopf bifurcation curve (namely, H_2) which delimits the stable injection-locking region below the so-called codimension-two saddle-node-Hopf point, in contrast to what has been reported for injected EEL [13]. We unveil period-doubling bifurcations (*PD*) which, in combination with H_2, explains the snakelike shape in the PS curve with two local minima of the switching power, in agreement with recent experimental mapping of polarization dynamics of a VCSEL with orthogonal optical injection [26–30]. On the route to polarization switching leading to injection locking, we closely investigate the role played by a torus bifurcation on a two-polarization-mode solution, which explains the onset of time-periodic dynamics at the relaxation oscillation (RO) frequency in the noninjected mode together with wave-mixing dynamics in the injected mode. We furthermore analyze the strong impact of two key VCSEL's parameters, the linewidth enhancement factor and the spin-flip relaxation rate, on the injection locking and the observed bifurcation mechanisms.

Our paper is organized as follows. In Sec. II we detail the rate equation model used in our numerical simulations and bifurcation continuation study. We investigate, in Sec. III, qualitatively different PS scenarios for selected detunings between master and slave lasers. A global analysis of bifurcations underlying PS and the associated nonlinear dynamics is performed in Sec. IV. The influence of the VCSEL linewidth enhancement factor on the overall bifurcation picture is presented in Sec. V and that of the spin-flip relaxation rate is discussed in Sec. VI. We summarize our main conclusions in Sec. VII.

II. RATE EQUATION MODEL

The optically injected VCSEL is modeled using an extension of the so-called SFM which takes into account the light polarization degree of freedom for a quantum well semiconductor laser [24]. We consider an injection configuration in which the polarization of the injected field is orthogonal to that of the free-running VCSEL. To this end, we chose the device parameters such that the free-running VCSEL emits a stable stationary mode LP along the x axis. A y-LP optical field is then coupled into the VCSEL cavity. The rate equation model is given by [22,23]

$$\frac{dE_x}{dt} = \kappa(1+i\alpha)(NE_x + inE_y - E_x) - i(\gamma_p + \Delta\omega)E_x - \gamma_a E_x, \tag{1}$$

$$\frac{dE_y}{dt} = \kappa(1+i\alpha)(NE_y - inE_x - E_y) + i(\gamma_p - \Delta\omega)E_y + \gamma_a E_y + \kappa_{inj}E_{inj}, \tag{2}$$

$$\frac{dN}{dt} = -\gamma_e[N(1+|E_x|^2+|E_y|^2)] + \gamma_e\mu - i\gamma_e n(E_yE_x^* - E_xE_y^*), \tag{3}$$

$$\frac{dn}{dt} = -\gamma_s d - \gamma_e n(|E_x|^2+|E_y|^2) - i\gamma_e N(E_yE_x^* - E_xE_y^*). \tag{4}$$

E_x and E_y represent the slowly varying components of the linearly polarized electric fields in, respectively, the x- and y-polarization directions. Two carrier variables N and n are considered. The variable N is related to the total inversion between conduction and valence bands while n accounts for the difference in the carriers numbers of the two sublevels with opposite spins as proposed by the SFM model [25]. Amplitude anisotropy is modeled through linear dichroism γ_a and phase anisotropy is modeled by the linear birefringence γ_p. The other internal VCSEL parameters are defined as follows: κ is the optical field decay rate, γ_e is the decay rate of N, γ_s is the spin-flip relaxation rate, and α is the linewidth enhancement factor. Electrical pumping is represented by μ which is the normalized injection current ($\mu=1$ at threshold). External optical injection is modeled through κ_{inj}, E_{inj}, and $\Delta\omega$. κ_{inj} is the coupling coefficient, E_{inj} is the injected field amplitude, and $\Delta\omega$ accounts for the frequency detuning between the master and the slave frequencies. The detuning is defined as the difference between the frequency of the injected field, ω_{inj}, and the mean, ω_{int}, of the frequencies of x- and the y-LP modes [$\omega_{int}=(\omega_x+\omega_y)/2$] [25].

We have performed our numerical simulations using the following parameter choice for the VCSEL: $\kappa=300$ ns^{-1}, $\gamma_p=30$ rad ns^{-1}, $\gamma_a=0.5$ ns^{-1}, $\gamma_e=1$ ns^{-1}, and $\mu=1.5$. However, the linewidth enhancement factor, α, as well as the spin-flip relaxation rate, γ_s, will be appropriately changed in order to analyze the effect of these key VCSEL's intrinsic parameters on the dynamical characteristics of the injected VCSEL. For each parameter set, the orthogonal optical injection configuration will be preserved, i.e., the VCSEL operating conditions are such that it exhibits a stationary x-LP solution in the absence of optical injection.

III. POLARIZATION SWITCHING SCENARIOS

We provide different bifurcation scenarios which are obtained by scanning the injection strength E_{inj} for selected frequency detuning values $\Delta\omega$ and for $\alpha=3$ and $\gamma_s=50$ ns^{-1}. At this stage, the rate equations are integrated using classical methods which give access to the dynamics of *only stable* solutions. The results are presented in Fig. 1 as bifurcation diagrams and reveal qualitatively different switching scenarios depending on the detuning. At each injection strength of the bifurcation diagram, the minima and maxima of polarization-resolved intensities, $I_{x,y}=|E_{x,y}|^2$, are plotted for a time series of 50 ns after waiting for the transient to die out and when increasing (left panels) and decreasing (right panels) the injection strength E_{inj}.

Figure 1 [(a1) and (a2)], which have been obtained for $\Delta\omega=72$ rad ns^{-1}, corresponds to a switching dynamics en-

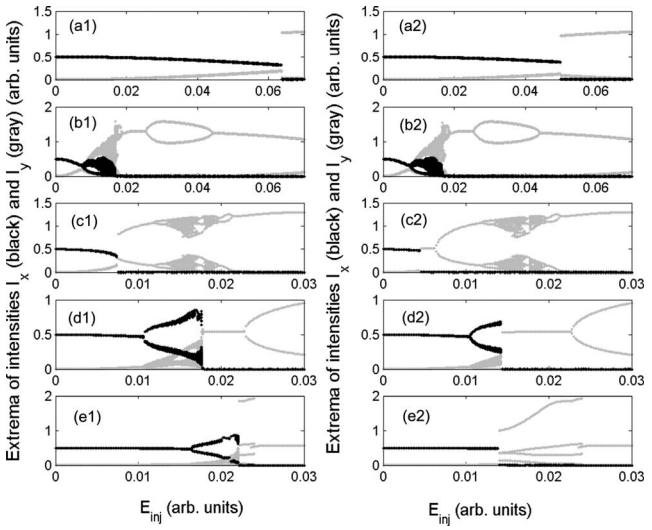

FIG. 1. Bifurcation diagrams of the LP mode intensities showing the different scenarios of PS for (a) $\Delta\omega=72$, (b) 30, (c) 23, (d) 10, and (e) -2.2 rad ns^{-1}. Left panels: injection strength is increased; right panels: injection strength is decreased. Black (gray) corresponds to x- (y-) LP mode. The linewidth enhancement factor is $\alpha=3$.

countered in the range of relatively large detuning values. In this region, the upward switchings from x to y (when increasing E_{inj}) as well as the downward switching from y to x (when decreasing E_{inj}) appear abruptly and show polarization bistability. A more detailed analysis of this regime is presented in Fig. 2 which provides samples of intensity time traces and spectra obtained for two discrete injection strength values corresponding to the dynamics before PS [see Fig. 2, (a1)–(a3)] and after PS [see Fig. 2, (b1)–(b3)]. Before PS the two LP modes exhibit a very small time-periodic modulation of a steady-state dynamics (this modulation is very weak and therefore it is not resolved in the figure). By contrast, after

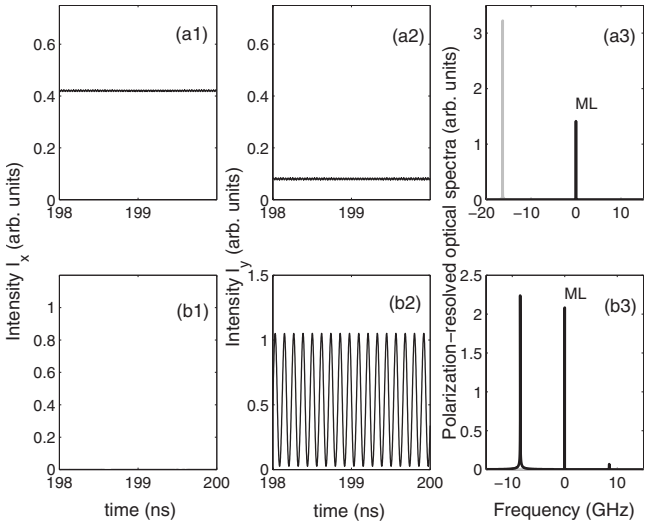

FIG. 2. Polarization-resolved intensities and optical spectra corresponding to the case of abrupt PS at $\Delta\omega=72$ rad ns^{-1} in Fig. 1(a). (a) $E_{inj}=0.04$, before PS; (b) $E_{inj}=0.07$, after PS. In the spectra black (gray) corresponds to y- (x-) LP mode.

PS the x-LP mode is switched off and the y-LP mode intensity exhibits a time-periodic dynamics at a frequency close to the detuning frequency between slave and master lasers [here $(72/2\pi)\approx 11.5$ GHz].

A more complex switching scenario is shown in Fig. 1 [(b1) and (b2)] for which the detuning has been set to $\Delta\omega=30$ rad ns^{-1}. The bifurcation diagrams in Fig. 1 [(b1) and (b2)] show that complicated time-periodic dynamics in the two LP modes may occur before PS is achieved. Unlike what has been shown in Fig. 1 [(a1) and (a2)], the upward PS is achieved in a rather progressive way and with almost no hysteresis. Intensity time-series and optical spectra are shown in Fig. 3 for selected injection strength values taken from Fig. 1 (b1). For a relatively weak injection strength E_{inj} [Fig. 3, (a1)–(a3)] the VCSEL emits predominantly in the x-LP mode. As we increase E_{inj}, the y-LP mode starts competing with the x-LP mode and the intensity at the master laser (ML) frequency increases at the expense of that in the x-LP mode. For larger E_{inj}, a bifurcation is crossed. It corresponds to the excitation of limit-cycle dynamics in both x- and y-LP modes [see Fig. 3, (b1)–(b3)]. It is worth noting that the two-mode time-periodic dynamics are achieved with a frequency close to the relaxation oscillation frequency f_{RO} [In our case $f_{RO}=(1/2\pi)\sqrt{2\kappa\gamma_e(\mu-1)}\approx 2.8$ GHz]. As E_{inj} is further increased, the two-mode periodic dynamics may then evolve in a more complex, possibly chaotic, dynamics [see Fig. 3, (c1)–(c3)]. Then the noninjected mode (x-LP) switches off and the injected VCSEL undergoes a period-doubling bifurcation which is then followed by a reverse period-doubling bifurcation [follow the evolution of the dynamics from Fig. 3(d3) to Fig. 3 (f3)] leading to a period-one limit-cycle regime involving only the y-LP mode [see Fig. 3 (f3)]. Interestingly, the numerically obtained switching scenario is in qualitative agreement with recent experimental results, i.e., when increasing the injection power, limit-cycle dynamics at the relaxation oscillations frequency in both x- and y-polarization modes are observed before achieving PS to a single mode time-periodic regime in the y-LP mode [29].

Another qualitatively different bifurcation scenario is illustrated in Fig. 1 [(c1) and (c2)] for $\Delta\omega=23$ rad ns^{-1}. The corresponding intensity time-series and optical spectra are shown in Fig. 4. In this case, by increasing E_{inj}, one induces an abrupt polarization switching which is then followed by a period-doubling route to chaos. In fact, when the injection strength is increased [Fig. 1 (c1)], PS is achieved from an unlocked x-LP to a y-LP time-periodic dynamics. As we still increase the injection strength, the time-periodic dynamics undergoes a period-doubling route to chaos. For larger injection strength, chaos is exited through a reverse period-doubling cascade. By then decreasing the injection power [Fig. 1 (c2)], a reverse scenario is obtained except that a region of injection-locking steady-state dynamics is now found before the VCSEL switches back to x-LP. Moreover, we notice that the reverse switching point occurs for a relatively lower injection level, thus showing the existence of bistability between an unlocked solution (with x-LP mode dominant) and a locked solution (y-LP only) steady-state dynamics. As it will be shown later (see Sec. IV), this bistable behavior results from the fact that, for such a detuning value

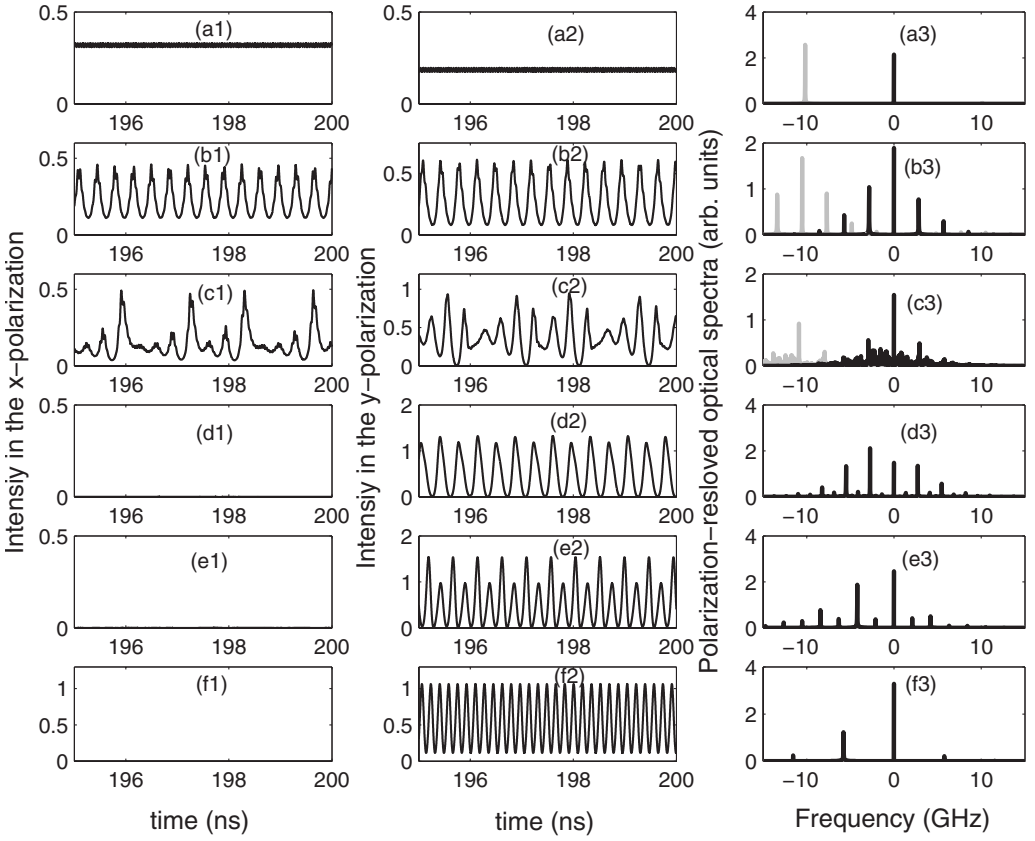

FIG. 3. Polarization-resolved intensities and optical spectra for a detuning of $\Delta\omega=30$ rad ns^{-1} corresponding to Fig. 1(b) and describing PS from a two-mode [*x*- and *y*-LP, Fig. 3(b)] to a single mode [*y*-LP, Fig. 3(d)] periodic dynamics. Before PS, the two-mode periodic dynamics develops into a more complex, almost chaotic regime as shown in Fig. 3(c). (a) $E_{inj}=0.007$, unlocked *x*-LP; (b) $E_{inj}=0.010$ quasiperiodic dynamics in *x*- and *y*-LP mode; (c) $E_{inj}=0.0145$, chaos in both *x*- and *y*-LP mode; (d) $E_{inj}=0.0185$, periodic *y*-LP mode; (e) $E_{inj}=0.035$, period-doubling, (f) $E_{inj}=0.07$ period-one dynamic after a reverse period-doubling bifurcation. In the spectra black (gray) corresponds to *y*- (*x*-) LP mode.

and by increasing E_{inj}, PS is achieved after crossing the Hopf bifurcation that delimits the injection-locking region. For a more insightful analysis of the dynamics described in Fig. 1(c), we present in Fig. 4 samples of polarization-resolved intensity time traces as well as optical spectra which have been obtained for selected injection strength values taken from Fig. 1 (c1) (except Fig. 4 [(b1)–(b3)] which correspond to an injected locked state from Fig. 1 (c2), i.e., when decreasing E_{inj}). The situation before PS is shown in Fig. 4 [(a1)–(a3)] for which the VCSEL exhibits an unlocked solution. For this small injection strength value the VCSEL emits predominantly in the *x*-LP mode. As the injection strength is increased, the VCSEL switches to *y*-polarization mode and undergoes a period-doubling route to chaos: a period-one limit cycle [Fig. 4, (c1)–(c3)] followed by a period-two [Fig. 4, (d1)–(d3)] which then leads to chaotic dynamics [Fig. 4, (e1)–(e3)]. Furthermore, it appears from spectral analysis that the limit cycle is excited with a frequency close to the RO. With our parameter choice, $f_{RO}=(1/2\pi)\sqrt{2\kappa\gamma_e(\mu-1)}\approx 2.8$ GHz, which is close to the frequency of the peaks on both sides of the master laser frequency (here $f_{ML}=0$ GHz since our equations are written in the reference frame of the master laser). As it will be shown in Sec. V, the observed period-doubling dynamics which follows PS denotes the existence of an injection-parameter region where the system is characterized by severe dynamical instabilities which depend strongly on the VCSEL linewidth enhancement factor (or α factor).

We next analyze the dynamics represented in Fig. 1 [(d1) and (d2)] for which the detuning has been set at $\Delta\omega=10$ rad ns^{-1}. A detailed description of the corresponding switching scenario is shown in Fig. 5, in which polarization-resolved intensity time traces and optical spectra are presented. In the relatively weak injection regime [Figs. 5(a)], the VCSEL emits predominantly in the *x*-LP mode with a very weak time-periodic modulation of the steady state. Interestingly, as the injection strength is increased and before PS occurs [Fig. 5, (b1)–(b3)], the slave VCSEL exhibits a well-resolved time-periodic dynamics, which does not appear in the previously investigated switching scenarios. As shown in Fig. 5 (b3), when the frequency offset between ML and the *y*-LP mode is close to the relaxation oscillations frequency, two peaks are excited on both sides of the main *x*-LP peak with a frequency offset close to f_{RO}. The *x*-LP mode therefore exhibits a time-periodic dynamics at the RO frequency. However, the optical spectrum corresponding to the *y*-LP mode shows a wave mixing between the *y*-LP slave laser main peak and the injected master laser field. Side peaks indeed appear at frequencies multiple of the frequency offset between the *y*-LP main peak and the master laser peak.

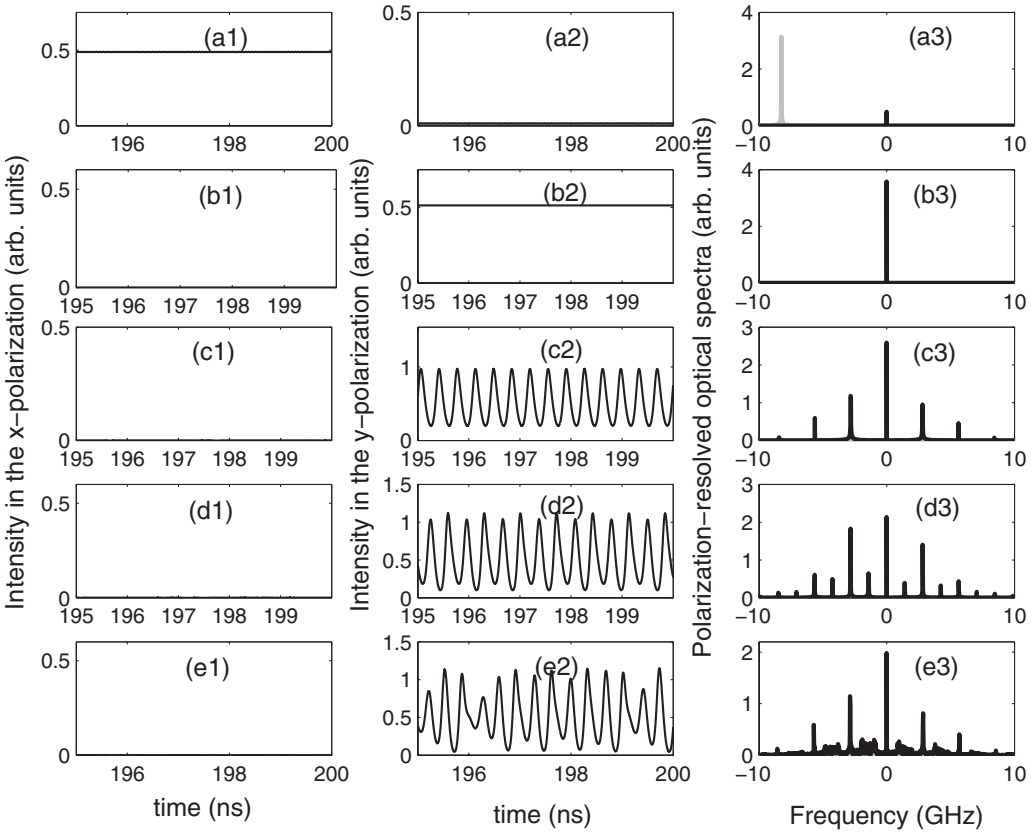

FIG. 4. Polarization-resolved intensities and optical spectra showing PS accompanied by a period-doubling route to chaos at $\Delta\omega=23$ rad ns^{-1} corresponding to Fig. 1(c). (a) $E_{inj}=0.0025$, unlocked x-LP; (b) $E_{inj}=0.0055$ (downward scan), injection locking to ML frequency; (c) $E_{inj}=0.0095$, switching to a y-LP periodic regime; (d) $E_{inj}=0.013$, period-doubling; (e) $E_{inj}=0.0155$, chaotic dynamics. In the spectra black (gray) corresponds to y- (x-) LP mode.

If the injection strength is further increased, an abrupt polarization switching leads to injection locking as shown in Fig. 5 [(c1)–(c3)]. For higher injection strength levels, the injection-locked state is exited through a Hopf bifurcation which corresponds to the onset of a limit-cycle dynamics at the relaxation oscillation frequency, as plotted in Fig. 5 [(d1)–(d3)]. In contrast to what has been shown in Fig. 5 [(b1)–(b3)], this limit-cycle dynamics emerges from the injection-locked y-LP steady state. The numerically obtained switching scenario is in qualitative agreement with experimental results [28], i.e., when increasing the injection power, limit-cycle dynamics in the noninjected mode and wave mixing dynamics in the injected mode are observed before PS accompanied by injection locking. In Sec. IV, we reveal that such a two-mode time-periodic dynamics is born from a torus bifurcation mechanism which appears before PS and injection locking.

Let us now investigate the dynamics depicted in Fig. 1 [(e1) and (e2)] for a frequency detuning of $\Delta\omega=-2.2$ rad ns^{-1}. Here we focus on a switching scenario in which, while increasing the injection strength, PS from two-polarization-mode time-periodic dynamics to single-mode time-periodic dynamics is achieved before injection locking of the VCSEL to ML. The details about this regime are shown in Fig. 6 for selected injection strengths taken from Fig. 1 (e1), i.e., when increasing the injection strength. For a relatively low injection strength, the VCSEL emits a single x-LP mode characterized by a weak time-periodic modulation [Fig. 6, (a1)–(a3)]. As the injection strength is increased and similarly to the above-mentioned dynamics described in Fig. 1 (d1) for $\Delta\omega=10$ rad ns^{-1}, limit-cycle and wave-mixing dynamics appear for the x- and the y-LP modes, respectively [Fig. 6, (b1)–(b3)]. By still increasing the injection strength, PS is achieved from the two-polarization-mode solution to a nearly pulsating time-periodic dynamics in the y-LP mode only [Fig. 6, (c1)–(c3)]. A further increase in E_{inj} then leads to injection locking to ML [Fig. 6, (d1)–(d3)]. It is worth noting that the obtained switching is qualitatively different from the scenario described in Fig. 1 [(c1) and (c2)] and detailed in Fig. 5 for which the switching is achieved from the two-polarization-mode time-periodic solution to an injection-locked y-LP steady state. If E_{inj} is decreased from the injection-locked state [Fig. 1 (e2)], a reverse scenario is found except that, unlike what is shown in Fig. 1 (d2) for $\Delta\omega=10$ rad ns^{-1}, the two-polarization time-periodic dynamics (in both x- and y-LP modes) is no longer observed. The backward switching to x-LP is achieved abruptly and shows a relatively large hysteresis. As it will be shown in the Sec. IV, the difference between the switching scenarios shown in Fig. 1 [(c1) and (c2)] and Fig. 1 [(e1) and (e2)] resides in the fact that, as one increases the injection strength for selected detunings, the switching can be achieved after or before the crossing of the saddle-node bifurcation which partly delimits the injection-

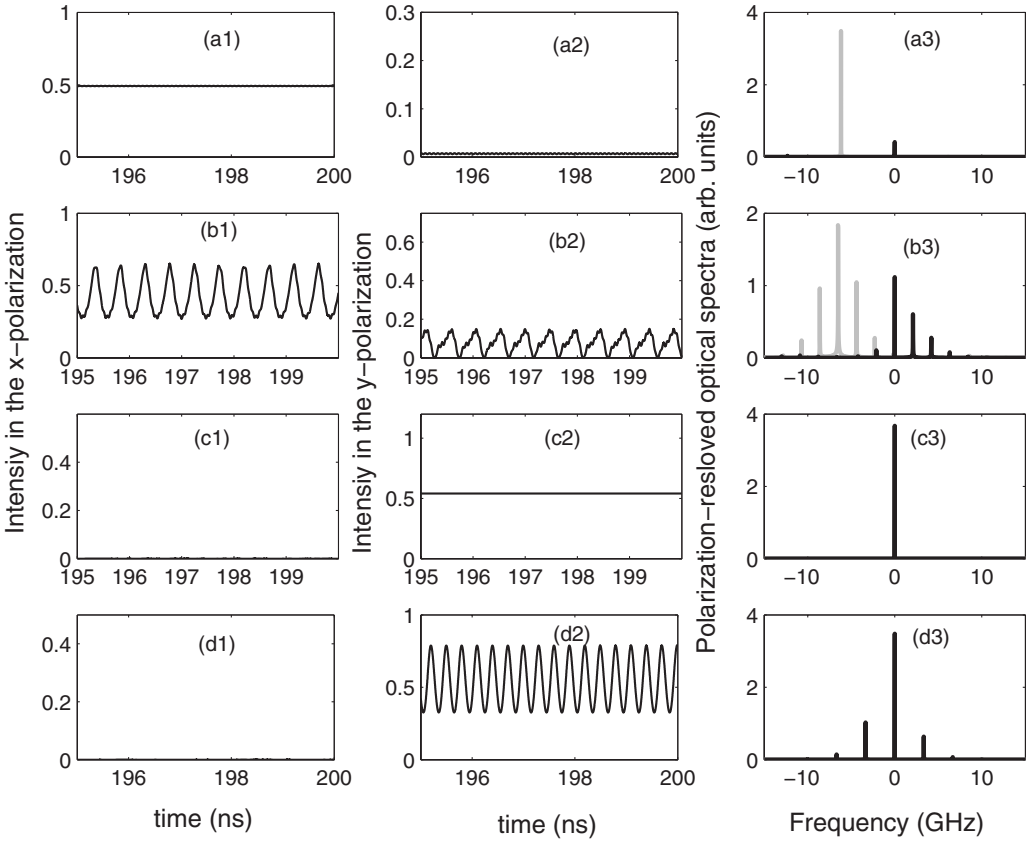

FIG. 5. Polarization-resolved intensities and optical spectra at $\Delta\omega=10$ rad ns^{-1} corresponding to Fig. 1(d) showing for: (a) $E_{inj}=0.005$, weak injection regime, (b) $E_{inj}=0.013$, excitation of limit cycle before PS for the x-LP mode and wave mixing between y-LP and ML; (c) $E_{inj}=0.020$, injection locking; (d) $E_{inj}=0.025$, limit cycle after crossing a Hopf bifurcation. In the spectra, black (gray) corresponds to y- (x-) LP mode.

locking zone in the $(E_{inj},\Delta\omega)$ bifurcation mapping.

IV. BIFURCATION AND POLARIZATION SWITCHING BOUNDARIES

We have so far presented different scenarios of PS dynamics by scanning the injection strength for fixed detuning values. In order to have a global understanding of how the PS interplays with the nonlinear laser dynamics resulting from Eqs. (1)–(4), in Fig. 7 we perform a mapping of bifurcation curves in the plane of the injection parameters $(E_{inj}, \Delta\omega)$ and for $\alpha=3$ and $\gamma_s=50$ ns^{-1}. Qualitative changes in the VCSEL dynamics are detected and followed using the continuation package AUTO 97 [31]. Different bifurcation curves are plotted: a saddle-node (*SN*), two Hopf (H_1 and H_2), and a torus (*TR*). We also report on two period-doubling bifurcation mechanisms denoted by PD_1 and PD_2. The supercritical and subcritical parts of each bifurcation curve are represented in black and gray, respectively. When increasing the injection strength, the VCSEL switches its polarization to that of the injected field. When decreasing the injection strength, the VCSEL switches back to its free-running polarization but for a smaller injection strength. These numerically computed "PS off" (x-LP mode off) and "PS on" (x-LP mode on) points are shown with circles and squares, respectively. The fact that PS on and PS off points do not occur for the same injected power and/or detuning makes clear the hysteresis associated to bistable PS.

The PS points, which are obtained by standard numerical integration, interplay with the bifurcation curves. *SN* and H_1 are bifurcations on a stationary injection-locked state and have also been reported in the case of optically injected EEL [13]. In the conventional case of EEL, the locking region is then delimited by the codimension two point G_1 where *SN* and H_1 become tangent. In our two-mode VCSEL system, the locking region is delimited by *SN* and H_1 but also by a bifurcation H_2. H_2 becomes tangent to SN at G_2, giving rise to a second codimension-two point G_2. The maximum detuning leading to injection locking therefore stays well below the codimension-two saddle-node-Hopf point G_1. The case of two G points has also been reported in single-mode EEL subject to optical injection [13], however, in the limit of small, close to zero, α and for large negative detuning and large injection strength. Moreover, the two G points in that case appear from the same H_1 bifurcation. Apart from its effect on the locking, H_2 also affects the polarization switching mechanism. The supercritical part of H_2 [see the bifurcation line which lies in between the G_2 and H_1-H_2 codimension-two points in Fig. 7(b)] coincides with PS on points, i.e., the switching on of the x-LP mode. Moreover, the smallest injection strength needed to achieve the switching off of the x-LP mode is located on H_2 and corresponds to

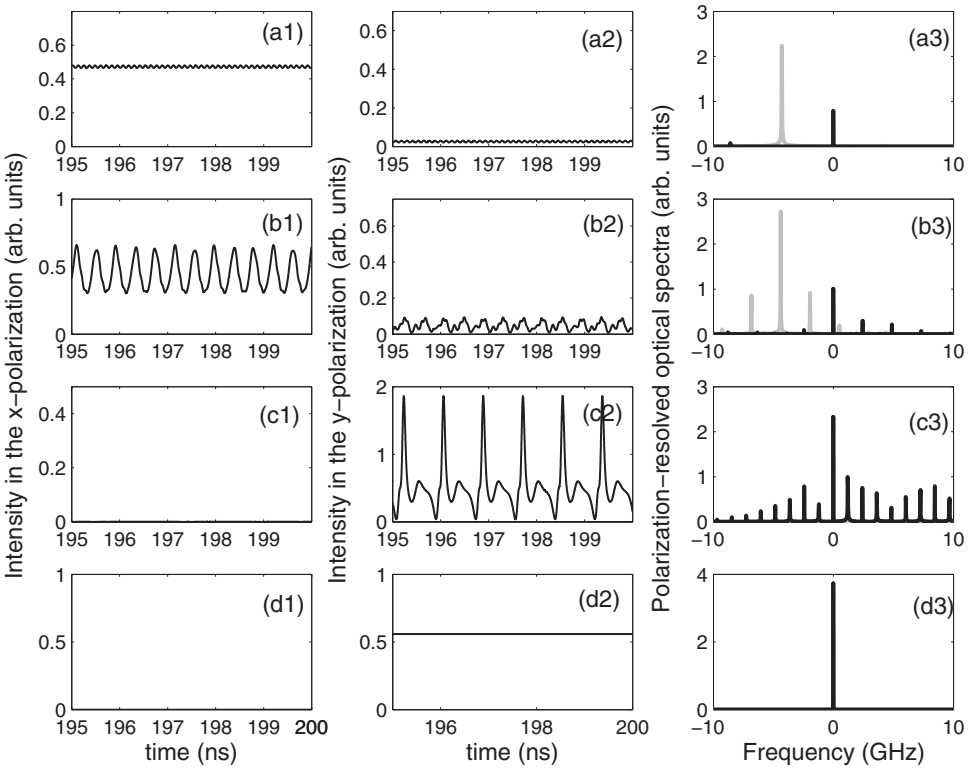

FIG. 6. Polarization-resolved intensities and optical spectra showing PS accompanied by a nearly pulsating regime for $\Delta\omega=-2.2$ rad ns^{-1}, corresponding to Fig. 1(e). (a) $E_{inj}=0.0150$, unlocked x-LP; (b) $E_{inj}=0.0188$, excitation of limit cycle before PS for the x-LP mode and wave mixing between y-LP and ML; (c) $E_{inj}=0.0230$, switching to a y-LP periodic regime; (d) $E_{inj}=0.0271$, injection locking. In the spectra black (gray) corresponds to y- (x-) LP mode.

a dramatic change in the polarization switching curve [see the point labeled m_1 in Fig. 7(c)]. This local minimum in the PS off is distinct but close to the H_1-H_2 codimension-two point.

In addition to H_2, our results reveal that the presence of chaotic attractors such as those bounded by PD_1 and PD_2 may affect the switching mechanism in a more intricate way. In fact the emergence of two regions of complex, possibly chaotic, dynamics delimited, respectively, by PD_1 and PD_2 coincides with the existence of the second local minimum denoted m_2 in Fig. 7(c). As a result, the PS curve exhibits a snakelike shape with local minima of the injected power required for the switching off of the x-LP mode [for details see Fig. 7(c); the broken line is used there as a guide for the eyes]. The observed snakelike shape and the role played by complex period-doubling mechanisms agrees qualitatively with previous experiments on VCSEL subject to orthogonal optical injection [26,27].

We have indicated by dotted lines in Fig. 7(a) the detuning values which correspond to the qualitatively different polarization switching scenarios described in Fig. 1. We show that for $\Delta\omega=72$ rad ns^{-1} [see also Fig. 1, (a1) and (a2)] the switching is achieved without being followed by injection locking or chaotic complex nonlinear dynamics. For $\Delta\omega=30$ rad ns^{-1} [see also Fig. 1, (b1) and (b2)] the regions of chaotic dynamics are crossed but not the injection-locking region. The case of an abrupt PS accompanied by injection locking and a period-doubling route to chaos is also shown for $\Delta\omega=23$ rad ns^{-1} [corresponding to Fig. 1, (c1)

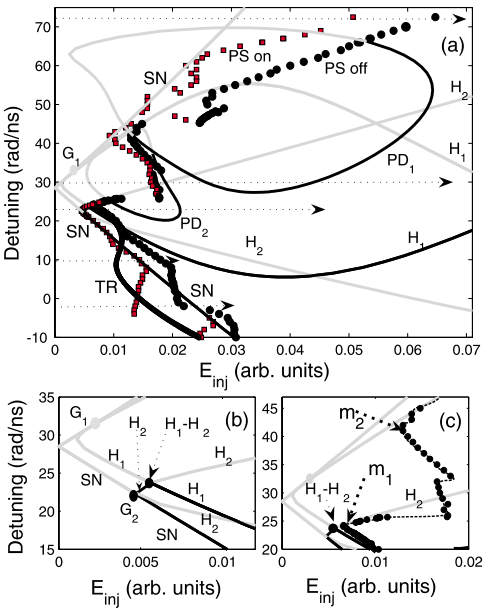

FIG. 7. (Color online) Bifurcation diagram in the plane $(E_{inj},\Delta\omega)$ (a). Horizontal dotted arrows indicate the switching scenarios detailed in Fig. 1. Close view of the codimension-two bifurcation mechanisms (b) and of the snakelike shape in the switching curve with local minima indicated by thick dotted arrows (c). Black (gray) denotes supercritical (subcritical) bifurcation. (TR; PS on; PS off) and (TR; PS on) curves have been removed, respectively, in panels (b) and (c) for clarity.

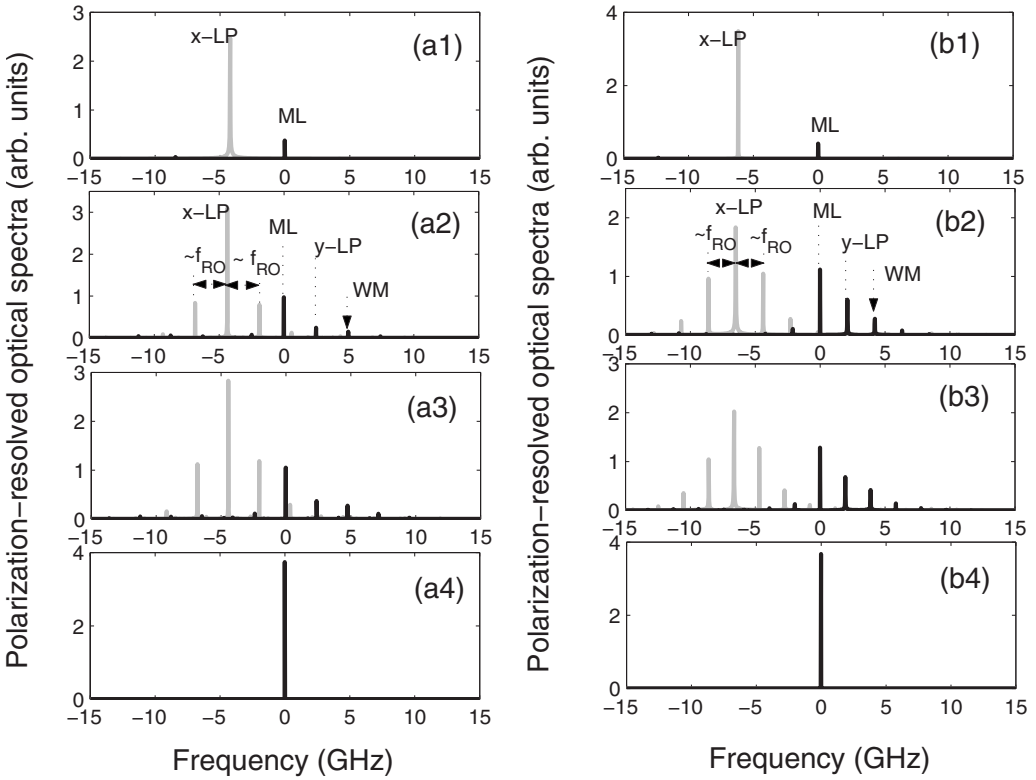

FIG. 8. Polarization-resolved optical spectra showing the dynamics leading to PS and locking when increasing the injection strength (from top to bottom) for (a1)–(a4) $\Delta\omega=-2.2$ rad ns^{-1} and (b1)–(b4) $\Delta\omega=10$ rad ns^{-1}. Black (gray) corresponds to y- (x-) LP mode.

and (c2)]. In this case both the injection-locking region and that of chaotic dynamics (bounded by PD_2) are crossed. However, the PS point when increasing E_{inj} is located after the H_1 bifurcation boundary [see Fig. 7(c) for details] and therefore injection locking is only observed when decreasing back the injection strength. Finally, the emergence of a relaxation oscillation dynamics in x-LP mode and wave mixing dynamics in y-LP mode before PS (see Fig. 1 [(d1) and (d2)] and Fig. 1 [(e1) and (e2)]) corresponds, in fact, to the torus bifurcation labeled *TR* in Fig. 7(a).

In order to investigate the role played by the torus bifurcation *TR* on the PS mechanism we revise the bifurcation scenarios presented in Fig. 1 [(e1) and (e2)] and Fig. 1 [(d1) and (d2)] for, respectively, $\Delta\omega=-2.2$ rad ns^{-1} [Fig. 8, (a1)–(a4)] and $\Delta\omega=10$ rad ns^{-1} [Fig. 8, (b1)–(b4)]. For a weak injection strength [see Fig. 8, (a1) and (b1) for $E_{inj}=0.005$], the VCSEL emits predominantly an unlocked x-LP mode. The optical spectrum of the x-LP mode shows one peak located at about the free-running detuning between master and x-LP mode, i.e., $f_x-f_{inj}=(-\gamma_p-\Delta\omega)/2\pi$. The optical spectrum of the y-LP mode shows one very small contribution at the master laser frequency (0 GHz). If the injection is further increased, we show that the crossing of *TR* coincides with the onset of time-periodic dynamics which involves both x- and y-LP modes [see Fig. 8 (a2) for $E_{inj}=0.0182$ and Fig. 8 (b2) for $E_{inj}=0.013$]. For the noninjected mode (x-LP), a limit-cycle dynamics at the RO frequency is excited. With our parameter set, the RO frequency is $f_{RO}=(1/2\pi)\sqrt{2\kappa\gamma_e(\mu-1)}\approx 2.8$ GHz which is close to the frequency offset of the two peaks located on both sides of the x-LP main peak. The spectrum of the injected-mode (y-LP) shows by contrast a wave-mixing dynamics between the y-LP mode and the ML. The y-LP mode frequency is initially detuned from the master frequency by $f_y-f_{inj}=(\gamma_p-\Delta\omega)/2\pi$. However, this frequency is pulled toward that of the master laser as the injection strength increases. The resulting y-LP frequency (labeled "y-LP") and the master laser frequency (labeled "ML") beat and give rise to new frequency components labeled "WM." For relatively larger injection levels [see Fig. 8 (a3) for $E_{inj}=0.0195$ and Fig. 8 (b3) for $E_{inj}=0.0145$], harmonics of the RO frequency is excited in the x-LP mode whereas we find, in the y-LP mode, spectral components with a frequency multiple of the frequency offset between ML and the y-LP mode. For sufficiently larger E_{inj}, polarization switching to an injection-locked single y-LP mode solution is achieved [see Fig. 8 (a4) for $E_{inj}=0.028$ and Fig. 8 (b4) for $E_{inj}=0.02$]. As it appears from the results obtained for two different detunings values [compare Fig. 8 (a2) to Fig. 8 (b2) and compare Fig. 8 (a3) to Fig. 8 (b3)], the TR bifurcation occurs when injection conditions (E_{inj} and $\Delta\omega$) are such that the frequency offset between the pulled y-LP mode and master laser is close to the RO frequency.

V. INFLUENCE OF THE LINEWIDTH ENHANCEMENT FACTOR α ON THE INJECTED VCSEL DYNAMICS

As it has been shown for EEL, the linewidth enhancement factor (α), which represents the phase-amplitude coupling, can dramatically influence the overall bifurcation mecha-

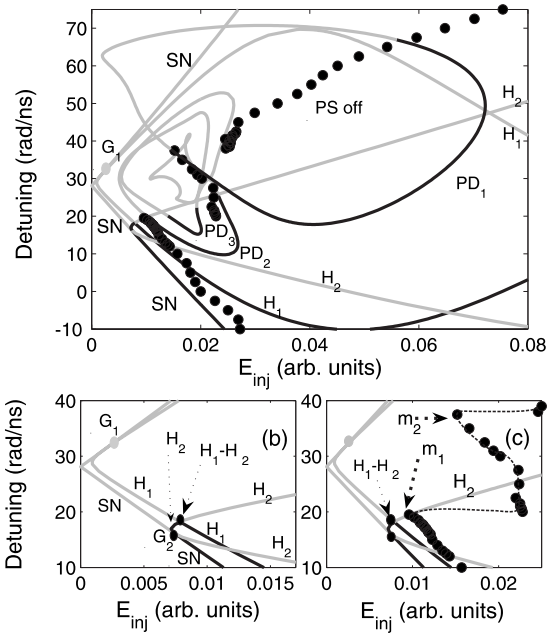

FIG. 9. Bifurcation diagram in the plane $(E_{inj},\Delta\omega)$ for $\alpha=3.75$. Black (gray) denotes supercritical (subcritical) part of each bifurcation curve. Bifurcation curves, codimension-two points, and switching points keep the same meaning as in Fig. 7.

nisms and is a key laser parameter in determining the nonlinear response of the optically injected semiconductor laser [13,32]. For the case of a VCSEL subject to orthogonal optical injection, one may expect a more intricate effect due to the polarization degree of freedom. In this section we analyze the effect of modifying the VCSEL α factor on the

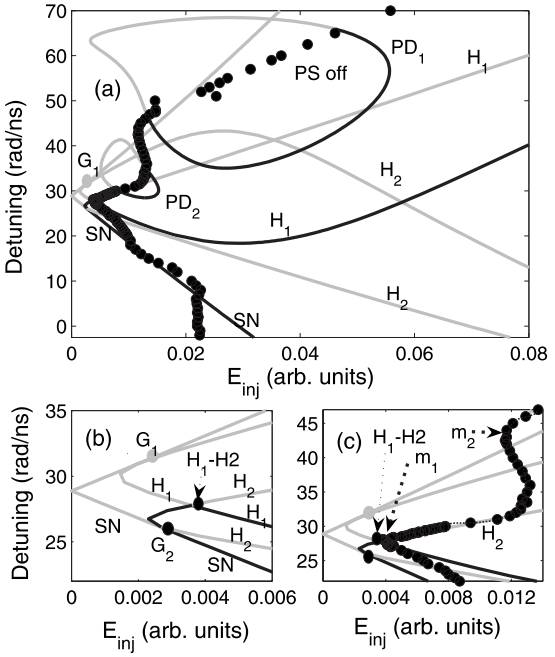

FIG. 10. Bifurcation diagram in the plane $(E_{inj},\Delta\omega)$ for $\alpha=2.25$. Black (gray) denotes the supercritical (subcritical) part of each bifurcation line. Bifurcation curves, codimension-two points, and switching points keep the same meaning as in Fig. 7.

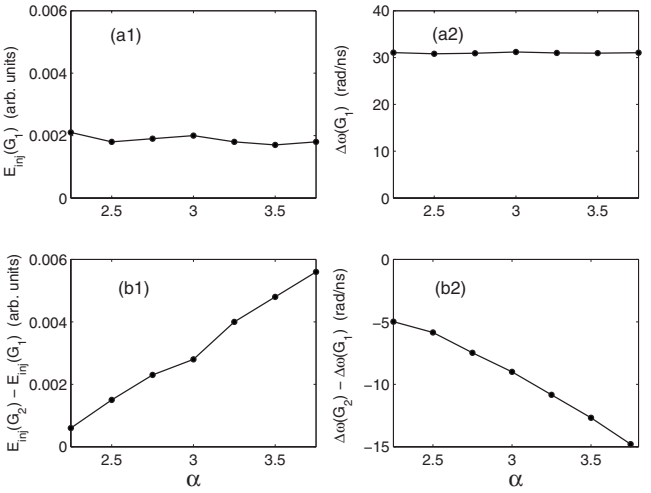

FIG. 11. Effect of the α factor on the positions of the G_1 and G_2 codimension-two points in the injection $(E_{inj},\Delta\omega)$ parameter plane.

bifurcation and PS boundaries. We plot in Figs. 9 and 10 the mappings corresponding to, respectively, $\alpha=3.75$ and $\alpha=2.25$ while $\gamma_s=50$ ns^{-1} (the same as in Secs. III and IV). For the sake of clarity, we represent only the PS off points, i.e., the switching points from the x-LP mode to y-LP mode when increasing the injection strength for fixed detunings. If we compare Figs. 7, 9, and 10, we find that the change in α affects the relative position between the different bifurcation curves and hence the location of the PS curve, the locking region, and the regions of complex chaotic dynamics. In the preceding section, we have reported on the existence of codimension-two points G_1 and G_2 arising from the intersection between the saddle-node bifurcation curve SN with, respectively, H_1 and H_2 Hopf bifurcation curves. The codimension-two point G_2 delimits the injection-locking region of the VCSEL and specifically originates from our two-mode problem. Our results suggest that to make its experimental observation easier it would be interesting to increase the detuning range between G_1 and G_2. Here, we study the dependence on the α factor of the position of G_1 and G_2 in the $(E_{inj},\Delta\omega)$ plane. In Fig. 11 [(a1) and (a2)] we present, respectively, the evolution with α of $E_{inj}(G_1)$ (the injection strength corresponding to G_1) and $\Delta\omega(G_1)$ (the detuning corresponding to G_1). Both Fig. 11 (a1) and Fig. 11 (a2) show that the location of G_1 on the mapping remains almost unchanged when varying α. We then analyze the evolution with α of $E_{inj}(G_2)-E_{inj}(G_1)$ [injection strength offset between G_2 and G_1, see Fig. 11 (b1)] and $\Delta\omega(G_2)-\Delta\omega(G_1)$ [the detuning offset between G_2 and G_1, see Fig. 11 (b2)]. We show that increasing α increases the injection strength and the detuning offsets between G_2 and G_1: as α is increased, G_2 is shifted toward larger negative detuning and higher injection strength levels with respect to G_1. In addition to the effect of α on the location of G_1 and G_2, we show that the smallest injection strength needed to achieve PS, when increasing the injection strength, is located on H_2 for all the three representative values of α [see the location of the minimum denoted by m_1 in Figs. 7(c), 9(c), and 10(c)].

We now closely investigate the consequence of the effect of α on the period-doubling bifurcations (and the associated

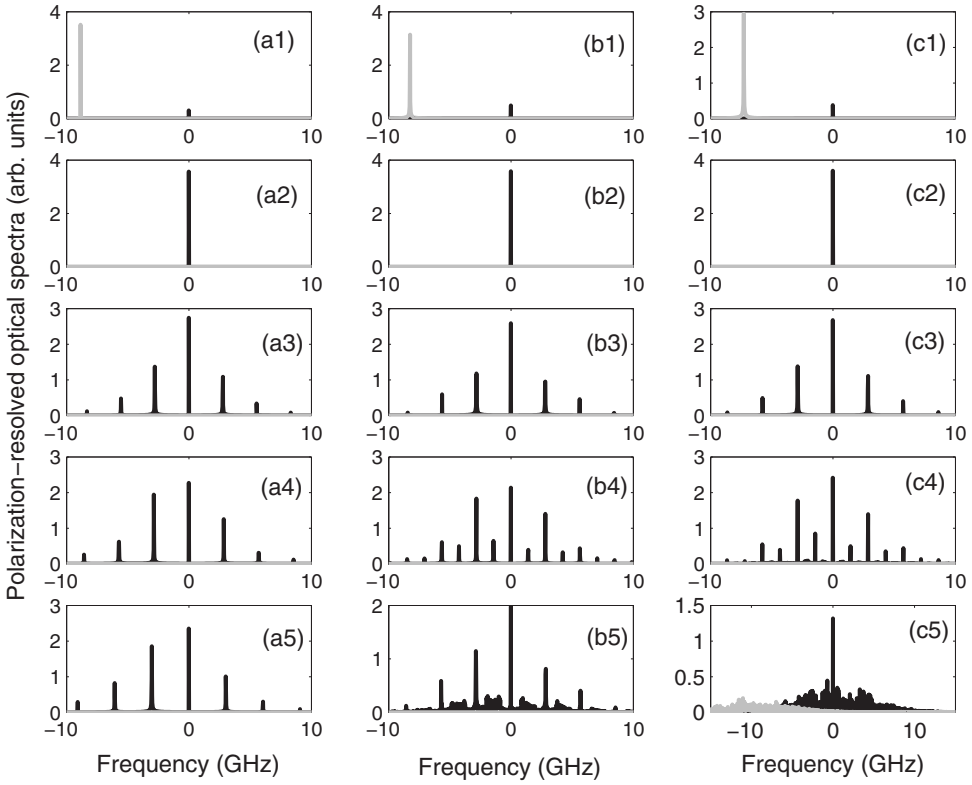

FIG. 12. Theoretical polarization-resolved optical spectra showing the dynamics leading to PS and locking when increasing the injection strength (from top to bottom) for: (a1)–(a5) $\alpha=2.25$ and $\Delta\omega=26.6$ rad ns^{-1}; (b1)–(b5) $\alpha=3$ and $\Delta\omega=23$ rad ns^{-1}; (c1)–(c5) $\alpha=3.75$ and $\Delta\omega=17.3$ rad ns^{-1}. Black (gray) corresponds to y- (x-) LP mode.

bubbles of chaotic instabilities). In agreement with what has been theoretically demonstrated in injected EEL, decreasing α may significantly shrink the injection parameter region over which complex nonlinear instabilities are observed [32]. In fact, if the linewidth enhancement factor is decreased from $\alpha=3$ (Fig. 7) to $\alpha=2.25$ (Fig. 10) with all other VCSEL's intrinsic parameters being kept the same, we find that the regions of complex nonlinear dynamics, bounded by the period-doubling curves PD_1 and PD_2, shrink in size. Moreover, in the smaller α case (see Fig. 10, $\alpha=2.25$) the initially overlapping period-doubling curves (see the relative position between PD_1 and PD_2 in Fig. 10) are now well separated in the $(\Delta\omega, E_{inj})$ mapping. Increasing α has an opposite effect (compare Fig. 7 for $\alpha=3$ and Fig. 9 for $\alpha=3.75$). In this case the regions of complex nonlinear dynamics bounded by PD_1 and PD_2 expand in size and their overlapping is significantly enhanced. We furthermore notice that the associated chaotic instability regions are now extended over a larger injection parameter range and may involve additional period-doubling mechanism which may lead to more complex chaotic dynamics. This is the case of Fig. 9 where, in addition to PD_1 and PD_2, a new period-doubling curve, denoted PD_3 is now resolved. Moreover, we find that the expansion of the PD bifurcation curves, due to the increase in α, dramatically affects the switching mechanism by decreasing the detuning range between the two local minima, m_1 and m_2, in the switching curve. Concretely, by increasing α, m_1 and m_2 are both achieved for smaller detunings and for larger injections strengths but this is accompanied by a decrease in the detuning range between them.

Here, we investigate the effect of the change in the α factor on nonlinear dynamics which accompanies the switching and locking mechanism. The results are presented in Fig. 12 where, for each value of α, the detuning is adequately chosen in such a way that we operate in between the saddle-node-Hopf (G_2) and the Hopf-Hopf (H_1-H2) codimension-two points, i.e., such that the supercritical part of H_2 is crossed when scanning E_{inj}. To this end, the selected detuning values are as follows: $\Delta\omega=26.6$ for $\alpha=2.25$ [see Fig. 12, (a1)–(a5)], $\Delta\omega=23$ for $\alpha=3$ [see Fig. 12, (b1)–(b5)], and $\Delta\omega=17.3$ rad ns^{-1} for $\alpha=3.75$ [see Fig. 12, (c1)–(c5)]. We represent the evolution of the dynamics of the injected VCSEL when increasing E_{inj} (except Fig. 12 [(a2), (b2), and (c2)]) which correspond to injected locked states, i.e., when decreasing E_{inj} from an initial state for which the VCSEL is operated in the higher-injection power regime and after the crossing of H_1 and PS off curves]. When the VCSEL operates in the relatively weak injection strength regime before achieving PS, [Fig. 12 (a1) for $\alpha=2.25$; Fig. 12 (b1) for $\alpha=3$; and Fig. 12 (c1) for $\alpha=3.75$], qualitatively similar dynamics is observed for the three values of α, i.e., the VCSEL predominantly emits an unlocked x-LP mode. Naturally the injection locking [Fig. 12 (a2) for $\alpha=2.25$; Fig. 12 (b2) for $\alpha=3$; and Fig. 12 (c2) for $\alpha=3.75$] and the limit-cycle period-one dynamics [Fig. 12 (a3) for $\alpha=2.25$; Fig. 12 (b3) for $\alpha=3$; and Fig. 12 (c3) for $\alpha=3.75$] are also similar. In the smaller alpha case ($\alpha=2.25$), one observes that increasing E_{inj} does not lead to destabilization of the limit-cycle period-one dynamics. Instead, only enhancement of the obtained limit cycle is observed [compare Fig. 12 (a3) for

E_{inj}=0.008; Fig. 12 (a4) for E_{inj}=0.0155; and Fig. 12 (a5) for E_{inj}=0.020]. However, for a larger alpha value (α=3), as the injection strength is increased, the limit-cycle period-one regime [Fig. 12 (b3) for E_{inj}=0.0095] undergoes a period-doubling [Fig. 12 (b4) for E_{inj}=0.0155] route to complex, possibly chaotic, instabilities [Fig. 12 (b5) for E_{inj}=0.020]. Similarly, for larger α value (α=3.75), a period-doubling route to chaos is also observed [Fig. 12 (c3) for E_{inj}=0.0119; Fig. 12 (c4) for E_{inj}=0.0137; and Fig. 12 (c5) for E_{inj}=0.0185]. The complexity of the chaotic dynamics increases as α is increased. Indeed, by comparing Fig. 12 (b5) and Fig. 12 (c5), one finds that the larger the α factor is the broader the spectrum of the chaotic regime becomes, which is indicative of a fully developed chaotic regime. Moreover, Fig. 12 (c5) shows that the VCSEL exhibits chaotic dynamics not only in the *y*-LP mode but also in the otherwise switched-off *x*-LP mode. This is in qualitative agreement with experimental results in Ref. [26] that show a bifurcation scenario for which PS is followed by period-doubling dynamics leading chaotic dynamics in *both* orthogonal fundamental LP modes.

VI. EFFECT OF THE SPIN-FLIP RELAXATION RATE γ_s ON THE DYNAMICS OF THE INJECTED VCSEL

Our intent is to analyze how nonlinear dynamics reported in the preceding sections are modified when considering larger values of the spin-flip relaxation rate γ_s. In fact, γ_s is a key parameter which, in the framework of the SFM model, accounts for several microscopic mechanisms responsible for the relaxation of the electron spin in quantum well semiconductor materials [24,25]. It is known from previous studies aiming at estimating γ_s through experimental measurements that the spin-flip relaxation rate strongly depends on the device under study [33–36]. It turns out that the magnitude of γ_s can span from few tens of ns^{-1} [33] to hundreds of ns^{-1} [34,35] or even very large values ($\gamma_s \to \infty$) [36]. The effect of γ_s on the dynamics of a VCSEL subject to optical injection has been numerically investigated in Ref. [23]. It was demonstrated that increasing γ_s can significantly shrink the region associated to the so-called elliptically polarized injection-locking solution and the underlying wave mixing dynamics in the detuning vs injection strength bifurcation map [22,23].

In order to highlight the effect of γ_s on the PS mechanism and nonlinear dynamics, we plot in Fig. 13 the bifurcation diagram for γ_s=100 ns^{-1}, i.e., twice the value of γ_s=50 ns^{-1} adopted in Secs. III and IV for a linewidth enhancement factor of α=3, all other VCSEL's intrinsic parameters being kept the same. We interestingly find that increasing γ_s affects the bifurcation map. By comparing Fig. 13(a) (for γ_s=100 ns^{-1}) and Fig. 7(a) (for γ_s=50 ns^{-1}), we find that only the second Hopf (H_2) and the torus (TR) bifurcations are affected by γ_s whereas the saddle-node (SN), the first Hopf (H_1), and the two period-doubling (PD_1 and PD_2) bifurcation boundaries are unchanged. Specifically, increasing γ_s shifts H_2 toward larger positive detunings. By analyzing Fig. 13(b) in light of Fig. 7(b), one finds indeed that the G_2 and H_1–H_2 codimension-two points (which determine the supercritical part of H_2, see Sec. IV) are shifted to larger positive detunings, thus leading to an expansion of the injection-locking region close to the so-called codimension-two point G_1.

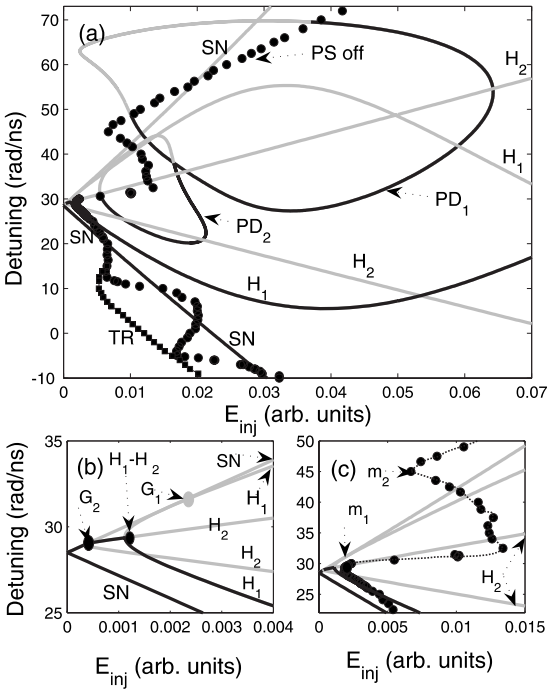

FIG. 13. Bifurcation diagram in the $(E_{inj}, \Delta\omega)$ parameter plane for α=3 and γ_s=100 ns^{-1}. Black (gray) denotes the supercritical (subcritical) part of each bifurcation line. Bifurcation curves, codimension-two points, and switching points keep the same meaning as in Fig. 7.

The effect of γ_s on H_2 is accompanied by significant changes in the switching mechanism. By comparing the positions of the PS curves denoted by "PS off" in Figs. 13(a) and 7(a), we first show that increasing γ_s results in an overall shift of both the switching curve and the torus bifurcation *TR* toward smaller injection strengths. In agreement with our conclusions in Sec. IV, we also unveil that the local minimum of the switching curve m_1, which corresponds to the smallest injection strength needed to achieve PS, is still located on H_2 [see Fig. 13(c)]. We furthermore show in Fig. 13(c) that, as a result of the interplay between PS and period-doubling dynamics, the switching curve still exhibits the snakelike shape with a second local minimum denoted m_2. It is worth noting the fact that though increasing γ_s has no effect on the areas of the map delimited by the period-doubling boundaries, the supercritical parts of both PD_1 and PD_2 bifurcation curves are extended over larger regions due to the overall shift of the PS curve [compare Figs. 13(a) and 7(a)].

We next follow how the Hopf bifurcation H_2 changes when sweeping γ_s over a relatively wide range (from γ_s=50 to γ_s=500 ns^{-1}). To this end we superimpose four bifurcation diagrams in the same $(E_{inj}, \Delta\omega)$ map as shown in Fig. 14 for four representative values: γ_s=50 (thick blue line), 75 (thick red line), 100 (thick black line), and 300 ns^{-1} (thick green line). For the sake of clarity, the distinction between supercritical and subcritical parts of the bifurcation

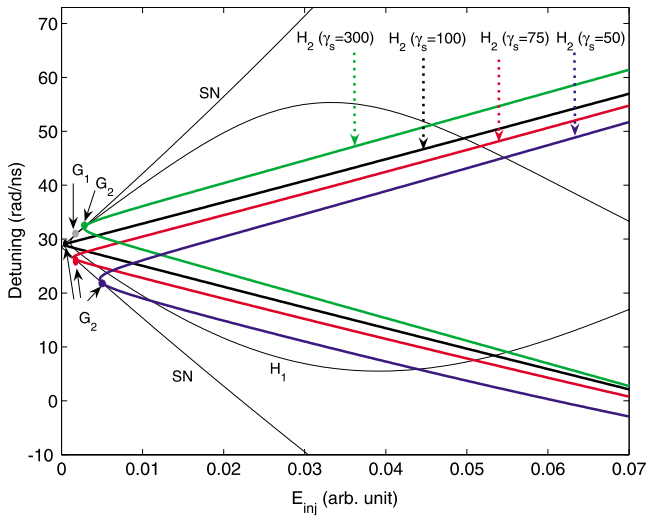

FIG. 14. (Color online) Effect of the spin-flip relaxation rate γ_s on the injected VCSEL dynamics for $\alpha=3$. Four bifurcation diagrams are superimposed in the same $(E_{inj},\Delta\omega)$ map. We show that the saddle-node (*SN*) and first Hopf (H_1) bifurcations do not change with γ_s while the second Hopf bifurcation H_2 does: $\gamma_s=50$ (thick blue line), $\gamma_s=75$ (thick red line), $\gamma_s=100$ (thick black line), and $\gamma_s=300$ ns^{-1} (thick green line). For clarity we do not distinguish between the supercritical and subcritical parts of the bifurcation lines (refer to Figs. 7, 9, 10, and 13 for details).

lines is omitted and the PS curve, *TR*, PD_1, and PD_2 bifurcations are not represented. As aforementioned, the saddle-node (*SN*) and the first Hopf (H_1) bifurcations do not change with γ_s while the second Hopf bifurcation H_2 does. In fact, increasing γ_s does not modify the shape of H_2 but the effect is rather an overall shift of the codimension-two point G_2 as already depicted in Fig. 13. Here, we furthermore show that for sufficiently large spin flip relaxation rates, e.g., $\gamma_s=300$ ns^{-1}, H_2 becomes completely subcritical. We have noticed from numerical simulations (not shown) that for large $\gamma_s>249.5$ ns^{-1}, the *x*-LP mode becomes unstable and the free-running VCSEL emits in the *y*-LP mode, in which case the injection scheme is no longer orthogonal.

Finally, the effect of γ_s on H_2 is quantitatively investigated in Fig. 15. To this end, we follow the evolution of relative position in the bifurcation diagram of the codimension-two point G_2 with respect to G_1 as a function of γ_s. As γ_s is progressively increased, we find

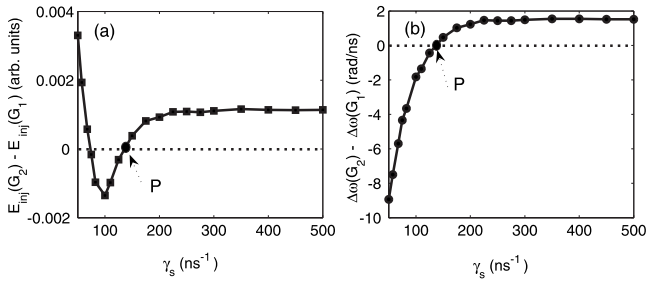

FIG. 15. Effect of the spin-flip relaxation rate γ_s on the relative position of G_2 with respect to G_1 codimension-two points in the injection $(E_{inj},\Delta\omega)$ parameter plane for $\alpha=3$.

that the injection strength offset between G_2 and G_1 $[\Delta E_{inj,G_1G_2}=E_{inj}(G_2)-E_{inj}(G_1)$, see Fig. 15(a)] exhibits a relatively sharp decrease, becomes zero and then negative as G_2 moves along *SN*. The curve has also a minimum corresponding to $E_{inj}(G_2)\approx 0$ which is obtained for $\gamma_s\approx 100$ ns^{-1}. If γ_s is further increased, G_2 moves toward G_1 such that they coincide at the point denoted *P* in Fig. 15(a) for $\gamma_s\approx 140$ ns^{-1}. Beyond *P*, $\Delta E_{inj,G_1G_2}$ increases with γ_s before it reaches a constant value for $\gamma_s>250$ ns^{-1}. Likewise, by anlyzing Fig. 15(b) [which shows the evolution of the detuning between G_2 and G_1, i.e., $\Delta\omega_{G_1G_2}=\Delta\omega(G_2)-\Delta\omega(G_1)$], we find that for $\gamma_s>250$ ns^{-1}, $\Delta\omega_{G_1G_2}$ is also constant, which means that H_2 does no longer depend on γ_s.

VII. CONCLUSIONS

In conclusion we have investigated in details the interplay between polarization and nonlinear dynamics in a VCSEL subject to orthogonal optical injection. We have identified the role played by a second Hopf bifurcation on the injection-locked solution (named H_2 in order to distinguish it from the well-known Hopf bifurcation typical to injected EEL that bounds the locking region). We have shown that H_2 delimits the stable locking zone below the codimension-two saddle-node-Hopf point, which clearly contrasts with what has been reported in the case of injected EELs. Furthermore, a mapping of both bifurcation boundaries and PS boundaries in the plane of the injection parameters shows that H_2 determines the smallest injection strength needed to achieve PS, i.e., a minimum in the PS boundary. The PS boundary exhibits a snakelike shape curve which can therefore be attributed to the combined effect of H_2 and period-doubling bifurcations leading to chaotic dynamics. By scanning the injection strength for particular detuning values, we obtain different polarization switching scenarios corresponding to bifurcations which qualitatively agree with recent experimental measurements [26,28,29]. Finally, we show that two key VCSEL's parameters, namely, the linewidth enhancement factor (α factor) and the spin-flip relaxation rate (γ_s), may strongly modify the overall bifurcation and polarization switching picture, while still preserving our general conclusions on the role played by H_2 bifurcation boundary and the snakelike shape PS boundary. Therefore, our study reveals bifurcation mechanisms resulting from the two-mode polarization dynamics of VCSELs and how the polarization switching properties of VCSELs are influenced by these emerging nonlinear dynamics. Such a complex interplay between bistable polarization switching properties and possibly two-polarization-mode chaotic dynamics is thought to be of great interest for recently suggested applications making use of polarization chaos for chaos secure communications [37–39].

ACKNOWLEDGMENTS

The authors acknowledge the support of Conseil Géneral of Région Lorraine, of COST Grant No. MP0702, of the FNRS, of BELSPO IAP Grant No. 6/10, of FWO-Vlaanderen, and of the OZR-VUB for the GOA and IOF projects.

[1] N. A. Olsson, H. Temkin, R. A. Logan, L. F. Johnson, G. J. Dolan, J. P. Van Der Ziel, and J. C. Campbell, IEEE J. Lightwave Technol. **3**, 63 (1985).
[2] P. Gallion, H. Nakajima, G. Debarge, and C. Chabran, Electron. Lett. **21**, 626 (1985).
[3] K. Iwashita and K. Nakagawa, IEEE J. Quantum Electron. **18**, 1669 (1982).
[4] X. Meng, T. Chau, and M. C. Wu, Electron. Lett. **34**, 2031 (1998).
[5] H. Kawaguchi, IEEE J. Sel. Top. Quantum Electron. **3**, 1254 (1997).
[6] S. C. Chan and J. M. Liu, IEEE J. Sel. Top. Quantum Electron. **10**, 1025 (2004).
[7] P. K. A. Wai, L. Xu, L. F. K. Lui, L. Y. Chan, and C. C. Lee, Opt. Lett. **30**, 1515 (2005).
[8] S. K. Hwang, J. M. Liu, and J. K. White, IEEE J. Sel. Top. Quantum Electron. **10**, 974 (2004).
[9] A. Gavrielides, V. Kovanis, M. Nizette, T. Erneux, and T. B. Simpson, J. Opt. B: Quantum Semiclassical Opt. **4**, 20 (2002).
[10] P. M. Varangis, A. Gavrielides, T. Erneux, V. Kovanis, and L. F. Lester, Phys. Rev. Lett. **78**, 2353 (1997).
[11] T. B. Simpson, J. M. Liu, K. F. Huang, and K. Tai, Quantum Semiclassic. Opt. **9**, 765 (1997).
[12] E. K. Lee, H. S. Pang, J. D. Park, and H. Lee, Phys. Rev. A **47**, 736 (1993).
[13] S. Wieczorek, B. Krauskopf, and D. Lenstra, Opt. Commun. **172**, 279 (1999).
[14] S. Wieczorek, B. Krauskopf, and D. Lenstra, Opt. Lett. **26**, 816 (2001).
[15] S. Wieczorek, B. Krauskopf, and D. Lenstra, Opt. Commun. **183**, 215 (2000).
[16] K. Iga, IEEE J. Sel. Top. Quantum Electron. **6**, 1201 (2000).
[17] K. D. Choquette, R. P. Schneider, K. L. Lear, and R. E. Leibenguth, IEEE J. Sel. Top. Quantum Electron. **1**, 661 (1995).
[18] J. Sacher, D. Baums, P. Panknin, W. Elsasser, and E. O. Gobel, Phys. Rev. A **45**, 1893 (1992).
[19] Z. G. Pan, S. Jiang, M. Dagenais, R. A. Morgan, K. Kojima, M. T. Asom, and R. E. Leibenguth, Appl. Phys. Lett. **63**, 2999 (1993).
[20] K. Panajotov, F. Berghmans, M. Peeters, G. Verschaffelt, J. Danckaert, I. Veretennicoff, and H. Thienpont, IEEE Photon. Technol. Lett. **11**, 985 (1999).
[21] Y. Onishi, N. Nishiyama, C. Caneau, F. Koyama, and C. E. Zah, IEEE Photon. Technol. Lett. **16**, 1236 (2004).
[22] M. Sciamanna and K. Panajotov, Opt. Lett. **30**, 2903 (2005).
[23] M. Sciamanna and K. Panajotov, Phys. Rev. A **73**, 023811 (2006).
[24] M. San Miguel, Q. Feng, and J. V. Moloney, Phys. Rev. A **52**, 1728 (1995).
[25] J. Martin-Regalado, F. Prati, M. San Miguel, and N. B. Abraham, IEEE J. Quantum Electron. **33**, 765 (1997).
[26] I. Gatare, M. Sciamanna, J. Buesa, H. Thienpont, and K. Panajotov, Appl. Phys. Lett. **88**, 101106 (2006).
[27] J. Buesa Altés, I. Gatare, K. Panajotov, H. Thienpont, and M. Sciamanna, IEEE J. Quantum Electron. **42**, 198 (2006).
[28] I. Gatare, M. Sciamanna, M. Nizette, and K. Panajotov, Phys. Rev. A **76**, 031803(R) (2007).
[29] I. Gatare,M. Sciamanna, and M. Nizette, Proc. SPIE **6997**, 699713 (2008).
[30] M. Sciamanna, I. Gatare, and K. Panajotov, *Proceedings of the International Commission for Optics (ICO-21), Sydney, Australia, 2008*, p. 287.
[31] E. Doedel, T. Fairgrieve, B. Sandstede, A. Champneys, Yu. Kuznetsov, and X. Wang, AUTO 97: http://indy.cs.concordia.ca/auto/main.html
[32] S. K. Hwang and J. M. Liu, Opt. Commun. **183**, 195 (2000).
[33] M. Sondermann, M. Weinkath, T. Ackemann, J. Mulet, and S. Balle, Phys. Rev. A **68**, 033822 (2003).
[34] M. P. van Exter, M. B. Willemsen, and J. P. Woerdman, Phys. Rev. A **58**, 4191 (1998).
[35] R. F. M. Hendriks, M. P. van Exter, J. P. Woerdman, K. H. Gulden, and M. Moser, IEEE J. Quantum Electron. **34**, 1455 (1998).
[36] P. Besnard, M. L. Charès, and G. Stéphan, J. Opt. Soc. Am. B **16**, 1059 (1999).
[37] I. Gatare, M. Sciamanna, A. Locquet, and K. Panajotov, Opt. Lett. **32**, 1629 (2007).
[38] M. Sciamanna, I. Gatare, A. Locquet, and K. Panajotov, Phys. Rev. E **75**, 056213 (2007).
[39] M. W. Lee, Y. Hong, and K. A. Shore, IEEE Photon. Technol. Lett. **16**, 2392 (2004).